Phys. Status Solidi A **210**, No. 10, 2135–2145 (2013) / **DOI** 10.1002/pssa.201329206

physica status solidi pss a
www.pss-a.com
applications and materials science

Silicon solar cell electrical parameter measurements through quantitative lock-in carrierographic (photoluminescence) and thermographic imaging

Junyan Liu[1,2], **Alexander Melnikov**[1], **and Andreas Mandelis**[*,1]

[1] Center for Advanced Diffusion Wave Technologies (CADIFT), Mechanical and Industrial Engineering, University of Toronto, Toronto, Ontario MS5 3G8, Canada
[2] School of Mechatronics Engineering, Harbin Institute of Technology, Harbin 150001, P. R. China

Received 26 March 2013, revised 14 June 2013, accepted 14 June 2013
Published online 17 July 2013

Keywords imaging, photoluminescence, silicon, solar cells, thermography

[*] Corresponding author: e-mail: mandelis@mie.utoronto.ca, Phone: 416-978-5106, Fax: 416-266-7867

We demonstrate theoretically and experimentally quantitative long-pass filtered lock-in carrierography (LIC) or lock-in photoluminescence (LIP) imaging and perform comparisons with lock-in thermography (LIT) imaging of industrial Si solar cells. Optoelectronic LIP and thermoelectronic LIT imaging modalities are used for non-destructive, non-contact measurements of the electrical parameters of solar cells from images obtained at various external load resistances. It is shown that quantitative surface-averaged pixel brightness statistical distributions derived from near-infrared (NIR) LIP and mid-infrared LIT images can be used to measure, among other parameters, photogeneration current density, diode saturation current density, ideality factor, and maximum power photovoltage of a multi-crystalline Si solar cell. LIP images were found to have superior contrast and spatial resolution to the respective LIT images. The electrical parameter values measured from the images were found to be in very good agreement with each other and with electrical measurements (EM). The theory further allows for the generation of derivative diode saturation current density and ideality factor images.

1 Introduction The current–voltage characteristics of solar cells directly determine their solar energy conversion efficiency and can be described by the fundamental electrical parameters of the solar cell. Over the past 2–3 decades, many infrared radiometric methods have been used to evaluate the performance of solar cells, which include photothermal radiometry (PTR), lock-in thermography (LIT), photoluminescence (PL) imaging, and photocarrier radiometry (PCR), among others. PTR, the single-laser-beam counterpart of LIT is a powerful calorimetric tool for the determination of energy loss mechanisms and local electrical properties of solar cells. Other calorimetric techniques include thermistors and several photothermal generation methods: photoacoustic, laser beam deflection, and thermoreflectance detection [1–6]. LIT that includes dark lock-in thermography (DLIT) and illumination lock-in thermography (ILIT) is a useful characterization imaging technique widely used in solar cell research [6–15]. LIT is available for detection of shunts, series resistance and grain boundaries, and can be used to determine power loss based on appropriate calibration. PL imaging is a fast non-destructive and non-contact near-infrared (NIR) camera-based diagnostic method for detecting electronic defects associated with crystal imperfections in connection to the processing of solar cells [16–22]. Laser-induced PCR is dynamic spectrally gated frequency-domain PL, which has the advantage of filtering out the thermal infrared (non-radiative) component of the emission spectrum of de-exciting free photocarriers, and/or resolving the radiative versus the non-radiative components through spectrally windowed modulation frequency scans, thereby being sensitive only to radiative recombination events when performing dynamic measurements of transport properties in semiconductors [23]. Long-pass filtered lock-in photoluminescence imaging (LIPI), also known as lock-in carrierography (LIC) [24, 25], was recently developed to obtain a relationship between surface averaged

distributions of optoelectronic energy conversion efficiency and output photovoltage of Si solar cells on one hand, and modulated radiative-recombination emission images on the other [26].

In this paper, we explore additional quantitative aspects of LIT and LIPI imaging regarding solar cell properties beyond solar conversion efficiency [26]. We develop new theoretical relations between the radiative and non-radiative emission fluxes due to recombination of photocarriers (carrier density wave) and make connection to electrical parameters of the solar cell, namely the photogenerated current density J_g, saturation diode current density J_0, and ideality factor n. We describe the relation between LIT amplitude, the power loss flux, and a quantitative calibration expression for the LIT amplitude, all of which are used to obtain the aforementioned electrical parameters (J_g, J_0, and n) through measurements based on LIT images. Furthermore, a quantitative relation that links the radiative recombination emission flux to the electrical parameters of solar cells is developed and is used for the determination of the same fundamental parameters by means of LIPI measurements, while quality comparisons are made between LIT and LIPI imaging modalities. It is demonstrated that LIPI imaging can be used to produce derivative images of J_0 and n by means of the developed theory.

2 Theory Non-thermal radiation, as encountered in semiconductors under non-equilibrium conditions, has been described with the generalization of Planck's law as introduced by Würfel [27]. For optoelectronic semiconductor materials of band gap energy $E > 1$ eV, and small photovoltages such that $E - qV \gg k_B T$, where q is the elementary charge and $k_B T$ is thermal energy, the emitted photon flux has been accurately simplified as [26]

$$F_R(V,T) \cong \left[\left(\frac{\alpha(E)E^3}{4\pi^2\hbar^3c^2}\right)\exp\left(\frac{-E}{k_BT}\right)\right]\exp\left(\frac{qV}{k_BT}\right). \quad (1)$$

Here, $F_R(V,T)$ presents the radiative-recombination emission photon flux under non-equilibrium radiation conditions, $\alpha(E)$ is the absorption coefficient of the solar cell at the excitation wavelength and c is the speed of light in vacuum. Note that Eq. (1) assumes that no sub-bandgap light is absorbed. $\alpha(E)$ is related to non-thermal super-bandgap radiation and it is a function of excitation energy. Equation (1) does not include thermal photon emission and possible re-absorption.

The optoelectronic theory of solar cells [26] needs to be extended to yield a more comprehensive quantitative link between the photon flux due to radiative recombination and fundamental electrical parameters so as to allow for quantitative LIT imaging in addition to quantitative LIP imaging [26]. The extended theory further enables the construction of images of the saturation diode current density and ideality factor as derivative LIT and LIP images. For these purposes the following parameters are required in addition to those introduced in Ref. [26]: current collection efficiency, $\eta_{ce}[\hbar\omega, V(\hbar\omega), T]$, and incident and mean emission photon wavelengths, λ_{in} and λ_{em}. For LIP and LIT solar cell measurements made as shown in Fig. 1(a), the photocarrier flux can be described according to Fig. 1(b), and is given by

$$\eta F_i(\hbar\omega) = F_{rec}[\hbar\omega, V(\hbar\omega), T] + F_{ce}[\hbar\omega, V(\hbar\omega), T], \quad (2a)$$

where [26],

$$F_{rec}[\hbar\omega, V(\hbar\omega), T] = F_R[V(\hbar\omega), T] + F_{NR}[\hbar\omega_{NR}, V(\hbar\omega), T] - F_R(0,T). \quad (2b)$$

Here, η is the quantum efficiency for photogeneration of carriers by the absorbed photons; $F_i(\hbar\omega)$ and $F_{rec}[\hbar\omega, V(\hbar\omega), T]$ are the incident photon flux and the recombination photocarrier flux, respectively. Therefore,

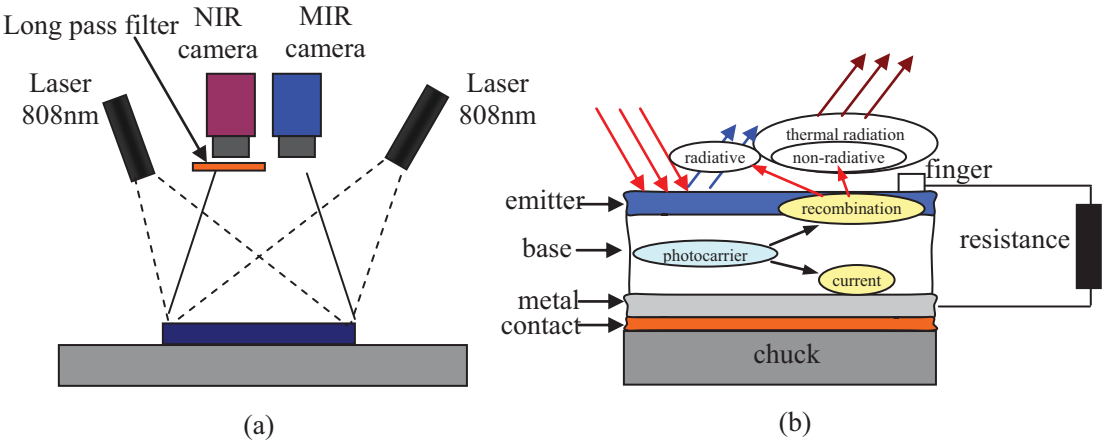

Figure 1 (a) LIT and LIC measurement set-up and (b) optical-to-photocarrier conversion channels.

$\eta F_i(\hbar\omega)$ has the meaning of the photogenerated carrier flux. F_{NR} is the heat flux resulting from the non-radiative conversion of optoelectronic to thermal energy [26]. $F_{ce}[\hbar\omega, V(\hbar\omega), T]$ is the photocarrier flux collected at the p–n junction that gives rise to the photocurrent. We further define $\eta_{ce}[\hbar\omega, V(\hbar\omega), T]$ to be the carrier collection efficiency, the ratio of the collected carrier flux to the photogenerated carrier flux

$$\eta_{ce}[\hbar\omega, V(\hbar\omega), T] = \frac{F_{ce}[\hbar\omega, V(\hbar\omega), T]}{\eta F_i(\hbar\omega)}. \tag{3}$$

When the incident photon energy is absorbed by the solar cell, energy conservation under short-circuit and open-circuit conditions, respectively, is described as follows:

$$\eta F_i(\hbar\omega)\hbar\omega_{in} = \left[\eta\eta_{ce}(\hbar\omega, 0, T)F_i(\hbar\omega)\hbar\omega_{in} + F_R(0, T)\hbar\omega_{em}\right]_{V(\hbar\omega)=0}, \tag{4a}$$

$$\eta F_i(\hbar\omega)\hbar\omega_{in} = \left[\eta\eta_{NR}(\hbar\omega, V_{OC}, T)F_i(\hbar\omega)\hbar\omega_{in} + F_R(V_{OC}, T)\hbar\omega_{em}\right]_{V(\hbar\omega)=V_{OC}}, \tag{4b}$$

where $\hbar\omega_{in}$ and $\hbar\omega_{em}$ are the incident photon energy and the mean radiative-recombination-emission photon energy, respectively, and η_{NR} is the quantum efficiency for non-radiative recombination [26]. η_{NR} and η_R, the quantum efficiency for radiative recombination, can be obtained at open-circuit from Eqs. (5a) and (5b),

$$\eta_{NR}(V_{OC}, T) = \frac{\eta_{ce}(\hbar\omega, 0, T) - \lambda_{in}\lambda_{em}^{-1}}{1 - \lambda_{in}\lambda_{em}^{-1}}, \tag{5a}$$

$$\eta_R(V_{OC}, T) = \frac{1 - \eta_{ce}(\hbar\omega, 0, T)}{1 - \lambda_{in}\lambda_{em}^{-1}}, \tag{5b}$$

where λ_{in}, λ_{em} are photon wavelengths corresponding to $\hbar\omega_{in}$ and $\hbar\omega_{em}$. The short-circuit (photogenerated) current density (bias voltage $V(\hbar\omega) = 0$) is obtained from Eq. (3),

$$J_g = qF_{ce}[\hbar\omega, 0, T] = q\eta\eta_{ce}(\hbar\omega, 0, T)F_i(\hbar\omega). \tag{6}$$

2.1 Lock-in thermography The possibility of determining the solar-cell current–voltage characteristics from an LIT amplitude image is based on the fact that the infrared thermal (blackbody) radiation is proportional to the dissipated power flux P_{loss} of the solar cell. Cahen et al. [1–4] have discussed in detail the dissipation mechanism for photovoltaic cells as measured by means of photoacoustic calorimetry. Breitenstein et al. [7] have calculated the dissipated thermal power density under monochromatic illumination as a function of bias voltage for a homogeneous solar cell. The dissipated power flux P_{loss} [W cm^{-2}] of a solar cell under monochromatic illumination is related to the photogenerated current density J_g, the injection current density J_D, the photovoltage $V(\hbar\omega)$, and the photon energy $\hbar\omega_{in}$ [1–4, 7]

$$P_{loss} = V(\hbar\omega)(J_D - J_g) + \hbar\omega_{in}F_i(\hbar\omega). \tag{7}$$

Furthermore, the injection current density depends exponentially on photovoltage,

$$J_D = J_0\left[\exp\left(\frac{qV(\hbar\omega)}{nk_BT}\right) - 1\right]. \tag{8}$$

Here, J_0 presents the saturation diode current density, and n is the electrical ideality factor. It should be noted that for harmonically modulated imaging modalities at angular frequency ω_M, such as in LIT and LIP imaging, complex quantities are implied with the general form $Z(\hbar\omega) = |Z(\hbar\omega)| \cdot e^{i\phi(\hbar\omega)} \cdot e^{i\omega_M t}$. In these cases magnitudes of dc quantities are replaced with amplitudes. Introducing the LIT amplitude mean-value as the signal obtained from illuminating the entire solar cell surface, the small signal temperature dependence becomes linear via the first order Taylor formula of the Stefan–Boltzmann law,

$$\langle|\mathrm{LIT}[V(\omega_M)]|\rangle = \frac{1}{S}\sum_{x=1}^{M}\sum_{y=1}^{N}|\mathrm{LIT}[V(\omega_M)]|_{x,y} \propto 4\sigma_e\varepsilon T_0^3[|T(\omega_M)| - T_0]. \tag{9}$$

Here, S is the illuminated surface area of the solar cell, $|T(\omega_M)|$ and T_0 are the modulated surface temperature amplitude and the ambient temperature, respectively; $V(\omega_M)$ denotes the modulated photovoltage peak value generated from irradiation at angular frequency ω_M; σ_e is the Stefan–Boltzmann constant; and ε is the surface emissivity. M and N are 320 and 256, respectively, corresponding to pixel numbers of both NIR and MIR cameras. The surface temperature of the solar cell is proportional to the dissipated power, and the proportionality factor can be identified as a calibration factor, C_{LIT} [3, 15],

$$\langle|\mathrm{LIT}[V(\omega_M)]|\rangle = C_{LIT}P_{loss}. \tag{10}$$

From Eqs. (4b) and (5a) it is found that the following relationship is valid at open-circuit:

$$C_{LIT} = \frac{\langle|\mathrm{LIT}(V_{OC})|\rangle}{|I_i|(1 - R)}\left(\frac{1 - \lambda_{in}\lambda_{em}^{-1}}{\eta_{ce}(\hbar\omega, 0, T) - \lambda_{in}\lambda_{em}^{-1}}\right), \tag{11}$$

where $|I_i|$ is the amplitude of the incident modulated illumination intensity and R is the surface reflectance. An expression for the surface-averaged LIT amplitude related to electrical parameters of the solar cell can be derived

from Eqs. (6)–(11):

$$\langle|\mathrm{LIT}[V(\omega_\mathrm{M})]|\rangle = A_0 V(\omega_\mathrm{M})\left[\exp\left(\frac{qV(\omega_\mathrm{M})}{nk_\mathrm{B}T}\right)-1\right] + A_\mathrm{g}[C - V(\omega_\mathrm{M})], \tag{12}$$

with

$$A_0 = C_\mathrm{LIT} J_0, \tag{13a}$$

$$A_\mathrm{g} = C_\mathrm{LIT} J_\mathrm{g}, \tag{13b}$$

$$C = \frac{\hbar\omega_\mathrm{in}}{q\eta\eta_\mathrm{ce}[\hbar\omega, 0, T]}. \tag{13c}$$

Assuming uniform surface reflectance across the solar cell, Eqs. (11)–(13) can be generalized for quantitative measurements of local electrical parameters in *inhomogeneous* solar cells:

$$|\mathrm{LIT}[V(\omega_\mathrm{M})]|_{x,y} = A_0(x,y)V(\omega_\mathrm{M})\left[\exp\left(\frac{qV(\omega_\mathrm{M})}{n(x,y)k_\mathrm{B}T}\right)-1\right] + A_\mathrm{g}(x,y)[C(x,y) - V(\omega_\mathrm{M})] \tag{14a}$$

and

$$C_\mathrm{LIT}(x,y) = \frac{|\mathrm{LIT}[V_\mathrm{OC}]|_{x,y}}{|I_\mathrm{i}|(1-R)}\left(\frac{1-\lambda_\mathrm{in}\lambda_\mathrm{em}^{-1}}{\eta_\mathrm{ce}[\hbar\omega,0,T]_{x,y} - \lambda_\mathrm{in}\lambda_\mathrm{em}^{-1}}\right). \tag{14b}$$

Finally, using Eqs. (11), (12) and (13), several fundamental electrical parameters of a solar cell (J_g, J_0, and n) can be accurately estimated by means of LIT imaging measurements (see Section 4).

2.2 Lock-in photoluminescence (carrierography)

Long-pass filtered LIP, or lock-in carrierography (LIC), is a non-contacting optoelectronic frequency-domain PL imaging method which has been applied to determine the solar conversion efficiency and photovoltage of industrial Si solar cells [26]. The LIP amplitude is proportional to the depth integral of the excess photogenerated carrier density wave, $N(z, \omega_\mathrm{M})$, over the thickness and it is equivalent to the spectral-bandwidth-integrated emission rate due to the radiative recombination of the excess photogenerated carriers. It should be mentioned that the mid-IR thermal-photon-emission-rate modulation frequency dependence also carries photocarrier recombination contributions [28]; however, the long-pass filtering of LIP eliminates these contributions. In LIP the influence of excess minority carrier reabsorption is negligible [23], as the absorption efficient for radiatively emitted luminescence photons is small, and so is the solar cell thickness. The radiative analog of Eqs. (9) and (10) can be written as

$$\langle|\mathrm{LIP}[V(\omega_\mathrm{M})]|\rangle = \frac{1}{S}\sum_{x=1}^{M}\sum_{y=1}^{N}|\mathrm{LIP}[V(\omega_\mathrm{M})]|_{x,y} \propto \int_0^L N(z,\omega_\mathrm{M})\mathrm{d}z, \tag{15a}$$

$$F_\mathrm{R}[\hbar\omega, V(\omega_\mathrm{M}), T] = C_\mathrm{LIP}\langle|\mathrm{LIP}[V(\omega_\mathrm{M})]|\rangle. \tag{15b}$$

It should be noted that the alternative term "carrierography imaging" stems from the source of the image signal which is a slice of the depth-integrated photoexcited free-carrier-density wave distribution lying within a modulation frequency-controlled f_M ($= \omega_\mathrm{M}/2\pi$) carrier diffusion length as indicated on the right-hand-side of Eq. (15a). From Eq. (15b) and the definition of radiative quantum efficiency, Eq. (5b), upon the introduction of an optoelectronic ideality factor n_j describing radiative recombination processes, as distinct from current generation processes which are described by n in Eq. (8), the following equations are obtained:

$$\eta\eta_\mathrm{R}(V_\mathrm{OC},T)F_\mathrm{i}(\hbar\omega) = C_\mathrm{LIP}[\langle|\mathrm{LIP}(V_\mathrm{OC})|\rangle - \langle|\mathrm{LIP}(0)|\rangle], \tag{16a}$$

$$F_\mathrm{R}(0,T)\left[\exp\left(\frac{qV(\hbar\omega)}{n_\mathrm{j}k_\mathrm{B}T}\right)-1\right] = C_\mathrm{LIP}[\langle|\mathrm{LIP}(V(\hbar\omega))|\rangle - \langle|\mathrm{LIP}(0))|\rangle]. \tag{16b}$$

A relationship between n_j and n can now be derived. From Eq. (16a), the relevant current–density-like quantities can be defined as

$$J[\hbar\omega, V(\hbar\omega), T]_\mathrm{R} = qC_\mathrm{LIP}[\langle|\mathrm{LIP}(V_\mathrm{OC})|\rangle - \langle|\mathrm{LIP}[V(\hbar\omega)]|\rangle], \tag{17a}$$

$$J_\mathrm{R} = q\eta\eta_\mathrm{R}(\hbar\omega, V_\mathrm{OC}, T)F_\mathrm{i}(\hbar\omega), \tag{17b}$$

$$J_\mathrm{R0} = qF_\mathrm{R}(0,T). \tag{17c}$$

From these definitions an equation can be obtained that is only related to the non-equilibrium radiative

recombination process,

$$J[\hbar\omega, V(\hbar\omega), T]_{\mathrm{R}} = J_{\mathrm{R}} - J_{\mathrm{R0}}\left[\exp(\frac{qV(\hbar\omega)}{n_{\mathrm{j}}k_{\mathrm{B}}T}) - 1\right], \quad (18)$$

where $J[\hbar\omega,V(\hbar\omega),T]_{\mathrm{R}}$ is defined as the non-equilibrium radiative recombination current density. Equation (18) can be compared to the conventional solar cell diode equation without series and shunt resistance:

$$J(V) = J_{\mathrm{g}} - J_0\left[\exp(\frac{qV}{nk_{\mathrm{B}}T}) - 1\right]. \quad (19)$$

Despite the formal similarity between Eqs. (18) and (19), the important difference is that the latter connects purely electrical quantities, whereas the former equation links the free carrier radiative recombination flux (current), an optically measurable quantity, to an electrical parameter. Unlike Eq. (10) in Ref. [26] which describes current density conservation rates and includes all photocarrier dissipation modes, Eq. (18) is related to the radiative recombination process alone, whence it carries a different optoelectronic ideality factor n_{j}. In Ref. [26] a detailed physical model was provided starting from the non-equilibrium radiation of the generalized Planck's and Kirchoff's laws linking the radiative emission flux to specific electrical parameters of solar cells. The model has a higher degree of detail in the explicit identification of the involved parameters than the simple relation between photovoltage and excess carrier density leading to PL reported by Trupke et al. [16] It thus allows the direct calculation of several fundamental electrical parameters (photogenerated current density, saturation diode current density, ideality factor) of a solar cell from the radiative emission (PL) rate. The derived relation, Eq. (18), between the photon emission flux due to radiative recombination in a solar cell is complementary to, and consistent with, the optoelectronic reciprocity approach by Kirchartz and Rau [29, 30]. Both approaches describe photocarrier-related photonic phenomena: the present treatment makes a connection between radiative (PL) flux, photocarrier recombination, and electrical parameters, while Kirchartz and Rau have developed a reciprocity relation between electroluminescent emission and photovoltaic quantum efficiency. Both phenomena are parts of photocarrier excitation and de-excitation pathways under different driving forces (light vs. electric fields).

From Eqs. (5b), (7), (15b), (16a), and (17b), the calibration factor and photogenerated current density are given by

$$C_{\mathrm{LIP}} = \frac{|I_{\mathrm{i}}|(1-R)\eta}{\hbar\omega_{\mathrm{in}}[\langle|\mathrm{LIP}(V_{\mathrm{OC}})|\rangle - \langle|\mathrm{LIP}(0)|\rangle]}\left(\frac{1-\eta_{\mathrm{ce}}(\hbar\omega,0,T)}{1-\lambda_{\mathrm{in}}\lambda_{\mathrm{em}}^{-1}}\right), \quad (20)$$

and

$$J_{\mathrm{g}} = qC_{\mathrm{LIP}}J_{\mathrm{R}}\left[\frac{1-\lambda_{\mathrm{in}}\lambda_{\mathrm{em}}^{-1}}{\eta_{\mathrm{ce}}(\hbar\omega,0,T)^{-1}-1}\right]. \quad (21)$$

The saturation diode current density is only related to the solar cell material properties [31] and is proportional to the background radiative recombination carrier flux. Assuming the radiative recombination quantum efficiency to be constant, from Eqs. (5b), (15b), and (17c) the saturation diode current density can be expressed as

$$J_0 = qC_{\mathrm{LIP}}J_{\mathrm{R0}}. \quad (22)$$

Equations (18) and (20) can also be generalized for quantitative measurements of optoelectronically inhomogeneous solar cells

$$C_{\mathrm{LIP}}(x,y) = \frac{|I_{\mathrm{i}}|(1-R)\eta}{\hbar\omega_{\mathrm{in}}\left[|\mathrm{LIP}(V_{\mathrm{OC}})|_{x,y} - |\mathrm{LIP}(0)|_{x,y}\right]} \times \left(\frac{1-\eta_{\mathrm{ce}}(\hbar\omega,0,T)}{1-\lambda_{\mathrm{in}}\lambda_{\mathrm{em}}^{-1}}\right), \quad (23a)$$

where

$$|\mathrm{LIP}(V_{\mathrm{OC}})|_{x,y} - |\mathrm{LIP}[V(\hbar\omega)]|_{x,y} = \frac{J_{\mathrm{R}}(x,y)}{C_{\mathrm{LIP}}(x,y)} - \frac{J_{\mathrm{R0}}(x,y)}{C_{\mathrm{LIP}}(x,y)}\left[\exp\frac{qV(\hbar\omega)}{n_{\mathrm{j}}(x,y)k_{\mathrm{B}}T} - 1\right]. \quad (23b)$$

As a byproduct of the formal similarity between Eqs. (18) and (19), a number of expressions can be derived. The most relevant quantities are the ideality factor relationship

$$n = n_{\mathrm{j}}\left[\frac{\ln\left(\frac{J_{\mathrm{R}}}{J_{\mathrm{R0}}}\right)}{\ln\left(\frac{J_{\mathrm{R}}}{J_{\mathrm{R0}}}\frac{\eta_{\mathrm{ce}}(\hbar\omega,0,T)}{\eta_{\mathrm{R}}}\right)}\right], \quad (24a)$$

and the open-circuit photovoltage

$$V_{\mathrm{OC}} \approx n\frac{k_{\mathrm{B}}T}{q}\ln\left(\frac{J_{\mathrm{g}}}{J_0}\right) = n_{\mathrm{j}}\frac{k_{\mathrm{B}}T}{q}\ln\left(\frac{J_{\mathrm{R}}}{J_{\mathrm{R0}}}\right), \quad (24b)$$

where n is the ideality factor of the solar cell, and n_{j} is the optoelectronic ideality factor related to radiative recombination processes. If $\eta_{\mathrm{R}} = 1$, then Eq. (5b) gives $\eta_{\mathrm{ce}} = \lambda_{\mathrm{in}}/\lambda_{\mathrm{em}}$ and n_{j} attains its maximum value ($<n$) since $\eta_{\mathrm{R}} + \eta_{\mathrm{NR}} = 1$ and the non-radiative channel does not extract any carriers ($\eta_{\mathrm{NR}} = 0$). Furthermore, if there is no energy loss during the conversion from incident to radiated photons (hypothetical), then $\eta_{\mathrm{ce}} = 1$ and $n_{\mathrm{j}} = n$: therefore, the diode behaves as more "ideal". An expression for the fill factor (FF) has been given by Ghosh et al. [32] and it can also be recast entirely in

terms of optoelectronic quantities associated with the present theory

$$\mathrm{FF} \cong \left[1 - \frac{1}{\ln\left(J_g/J_0\right)}\right]\left[1 - \frac{\ln\left[\ln\left(J_g/J_0\right)\right]}{\ln\left(J_g/J_0\right)}\right] \approx 1 - \frac{1}{\ln\left(\frac{J_R}{J_{R0}}\frac{1-\lambda_{in}\lambda_{em}^{-1}}{\eta_{ce}(\hbar\omega,0,T)^{-1}-1}\right)}. \quad (25)$$

3 Experimental details The first experimental applications of the foregoing theory are aimed at demonstrating that both LIT and LIP images are quantitative methods for estimating the electrical parameters of solar cells with data obtained by changing the external load resistance. The experimental setup is shown in Fig. 1(a). A mid-infrared camera (Cedip Titanium 550 from FLIR) with a 320 × 256 pixel active element, spectral bandwidth 2.5–5.0 μm, and frame rate 150 Hz for full window size was used for LIT measurements. An NIR camera (SU320KTSW-1, 7RT/RS170 from Goodrich Sensors Unlimited) with a long pass filter (~1000 nm) was used for LIC measurements. This camera has a 320 × 256 pixel active element, spectral bandwidth 0.9–1.7 μm, frame rate 119.6 Hz for full window size, and full-frame exposure times ranging from 0.13 to 16.6 ms. An industrial multicrystalline-Si solar cell (156 × 156 mm^2, 0.2 mm thickness) from Enfoton Solar Ltd., Cyprus, was used for both LIT and LIP measurements. It was illuminated from the front side using a superband-gap fiber coupled 16-W/808-nm diode laser. The laser beam was spread and homogenized by engineered microlens arrays forming a square illumination area with uniform intensity. For LIT and LIP measurements the illumination intensity was set at 0.043 and 0.038 W cm^{-2}, respectively (ca. 1/3 Sun). A data acquisition module from National Instruments was used to generate the modulation waveform for the laser current. The modulation frequency was set at 10 Hz, and the LIP and LIT amplitude and phase images were produced using in-house developed software.

To calculate the solar conversion efficiency and other electrical parameters, a series of load resistances were used to measure the *I–V* characteristics of our solar cell with dc illumination provided by the same 808-nm diode laser and conditions. The current I through the load resistance R_L and the photovoltage V across R_L were measured from electrical measurements (EM). The solar conversion efficiency was

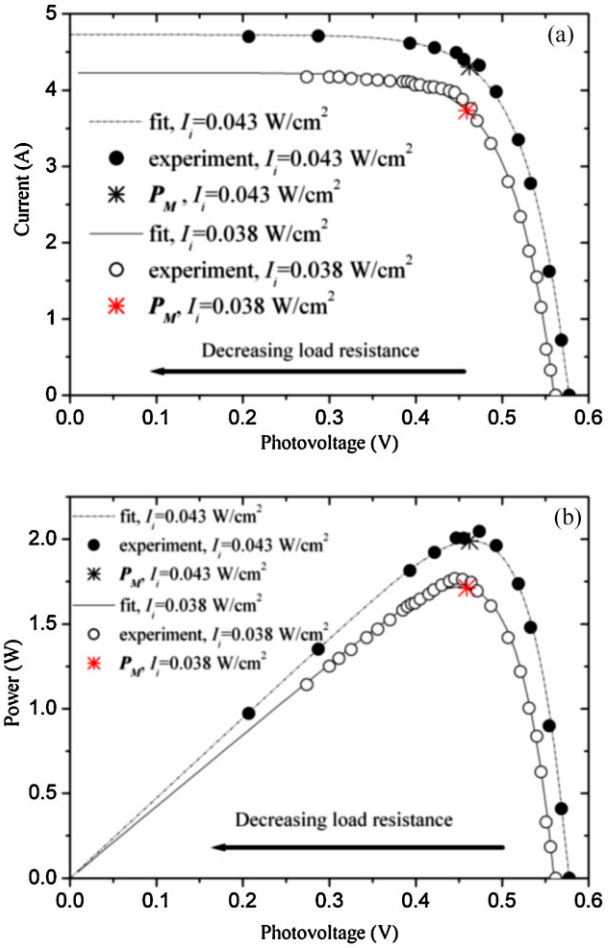

Figure 2 (a) *I–V* characteristics and (b) output power curve dependence on photovoltage. Illumination power density: 0.043 and 0.038 W cm^{-2}.

Table 1 Electrical parameters obtained by three methods.

parameters		I_i = 0.043 W cm^{-2}		I_i = 0.038 W cm^{-2}	
	method:	EM	LIT	EM	LIPI (LIC)
J_g (mA cm^{-2})		19.2	20.23	17.4	17.3
J_0 (μA cm^{-2})		0.169	0.156	0.117	0.124
ideality factor n		1.871	1.865	1.742	1.772
shunt resistance (Ω)		1000	—	1000	—
P_{max} voltage, V_{max} (V)		0.462	0.464	0.460	0.464
open-circuit voltage (V_{OC})		0.567	0.571	0.562	0.564
fill factor (FF)		0.7214	0.7234	0.7224	0.7211
solar conversion efficiency η_e (%)		18.3	19.4	18.6	18.7
R^2 (denotes best fit to eqs. used)		0.996	0.994	0.997	0.998

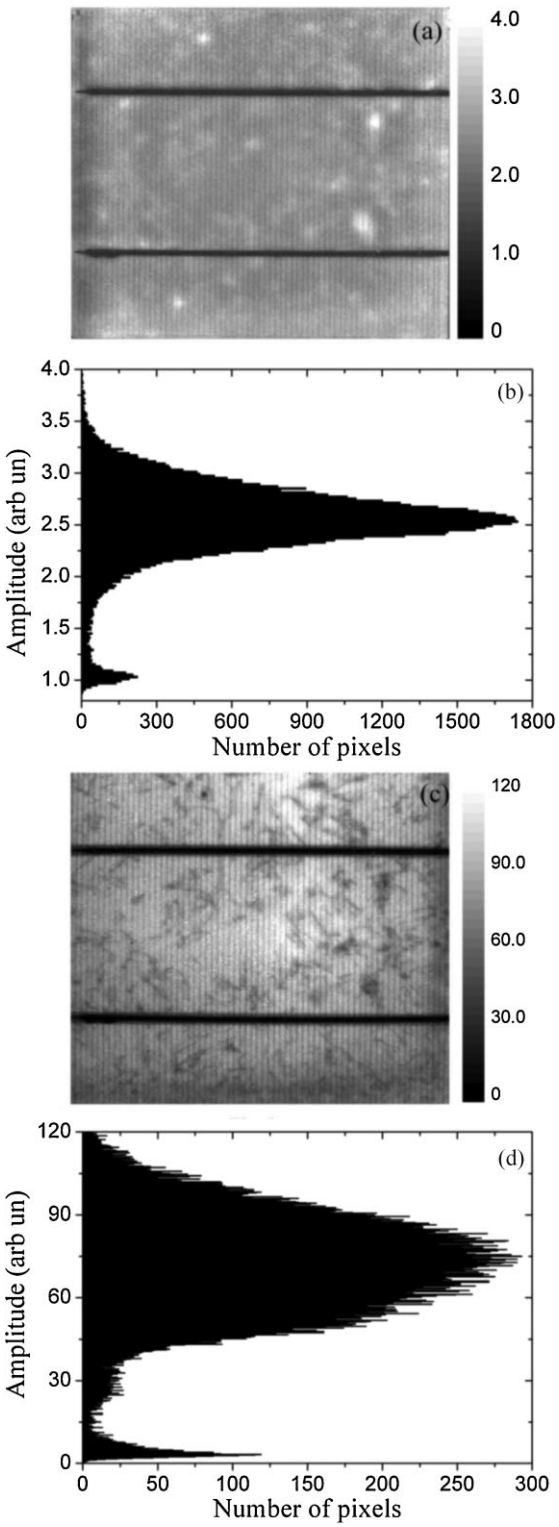

Figure 3 Amplitude image and statistical histograms of the whole solar cell under open-circuit at 10 Hz: (a), (b) LIT amplitude image and histogram of pixel brightness, illumination power density: 0.043 W cm^{-2}, bin size = 0.02 (denotes amplitude or phase values within a range x and $x + \Delta x$ (Δx: "bin size")). (c), (d) LIP amplitude image and histogram of pixel brightness, illumination power density: 0.038 W cm^{-2}, bin size = 0.25.

obtained from [31, 32]

$$\eta_e = \frac{V_m \times I_m}{J_i \times S} \times 100\%, \tag{26}$$

where V_m, I_m are the voltage and current at the maximum power point, J_i the incident light irradiance (mW cm^{-2}), and S is the surface area of the solar cell (cm^2).

4 Results and discussion The current–voltage characteristics, power output versus photovoltage curve and their theoretical best fits to the solar cell diode Eq. (19) without series resistance under dc-illumination are shown in Fig. 2. The values of the various electrical parameters were calculated and are shown in Table 1. The FF was calculated using FF = $P_{max}/(V_{oc}J_{sc}S)$. The photovoltages corresponding to maximum power, V_{pmax} = 0.462 V (I_i = 0.043 W cm^{-2}) and V_{pmax} = 0.460 V (I_i = 0.038 W cm^{-2}) were obtained from the peaks of the fitted curves in Fig. 2(b).

LIT and LIP amplitude images and their statistical histograms (camera pixel modulated brightness intensity

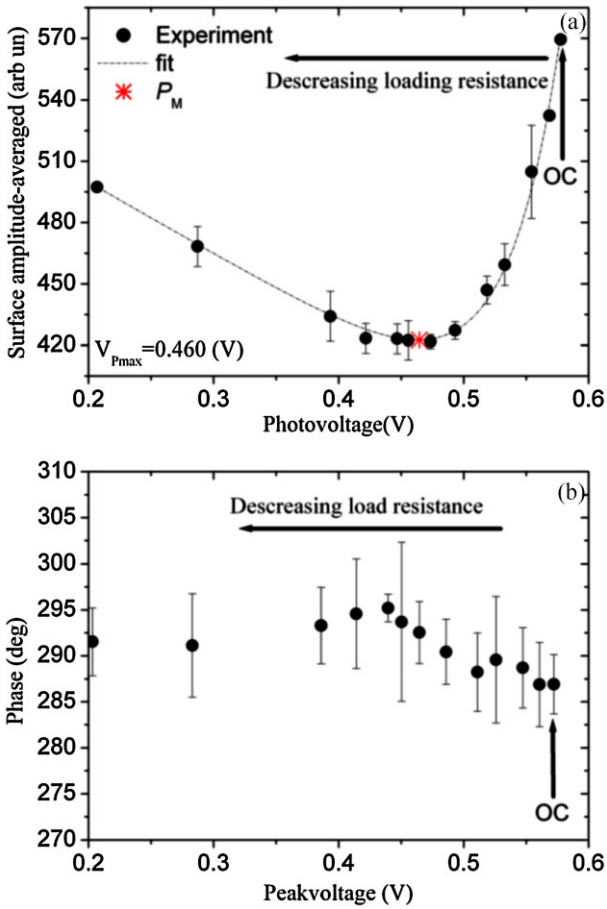

Figure 4 Surface-averaged (a) amplitude and (b) phase of LIT image pixel brightness statistical distribution dependence on photovoltage. In (a) surface-averaged amplitude was best-fitted to Eq. (12). Illumination power density: 0.043 W cm^{-2}, modulation frequency of 10 Hz.

distributions [26]) over the fully illuminated surface at open-circuit are shown in Fig. 3. Statistical histograms were obtained from all LIT and LIP amplitude images for the purpose of validating the foregoing theory with respect to quantitative dependencies of image pixel averages on solar conversion efficiency. Details of this methodology have been described in Ref. [26]. Figure 3(a) shows the thermal contrast due to an inhomogeneous distribution of non-radiative processes (heat flux) by dissipated power generation across the solar cell. From Fig. 3(b) the LIT amplitude image histogram at 10 Hz is peaked at approximately 2.5 (arbitrary units). The narrow amplitude peak at or near 1 is due to the light reflecting nature of the contacting electrodes, which prevent laser light from becoming absorbed and converted to either heat or radiation. Figure 3(c) shows the LIP imaging contrast due to the inhomogeneous distribution of radiative recombination process across the solar cell. It is observed that there exists a strong anti-correlation between peak emitting regions in the two images, as expected from energy conservation arguments between radiative and non-radiative de-excitation processes. It is also clear that the spatial resolution and contrast of the LIP image is superior to that of the LIT image. This is due to the long thermal diffusion length $\mu(\omega_M) = \sqrt{2\alpha/\omega_M}$ associated with LIT at 10 Hz (α: thermal diffusivity) which causes blurring. The LIC image spatial resolution and contrast are controlled by the much shorter carrier diffusion length $L_C(\omega_M) = \sqrt{D\tau/(1+i\omega_M\tau)} \approx \sqrt{D\tau}$ at 10 Hz, where D is the electronic diffusivity and τ is the effective recombination lifetime of the photogenerated carriers. Very low values of τ in the optoelectronically low-quality regions and grain boundaries result in $L_C \ll \mu$ which enhances LIP spatial resolution at the expense of decreased signal-to-noise ratio. The LIP amplitude image histogram at 10 Hz, Fig. 3(d), is more broadened than the LIT pixel distribution, peaking at approximately 75 (arbitrary units). The broadened pixel distribution is indicative of the higher spatial resolution of the LIP image compared to the LIT image, Fig. 3(a). The narrow amplitude peak at or near zero is due to very low pixel readings contributed from regions on or near the contacting electrodes, similar to the LIT distribution.

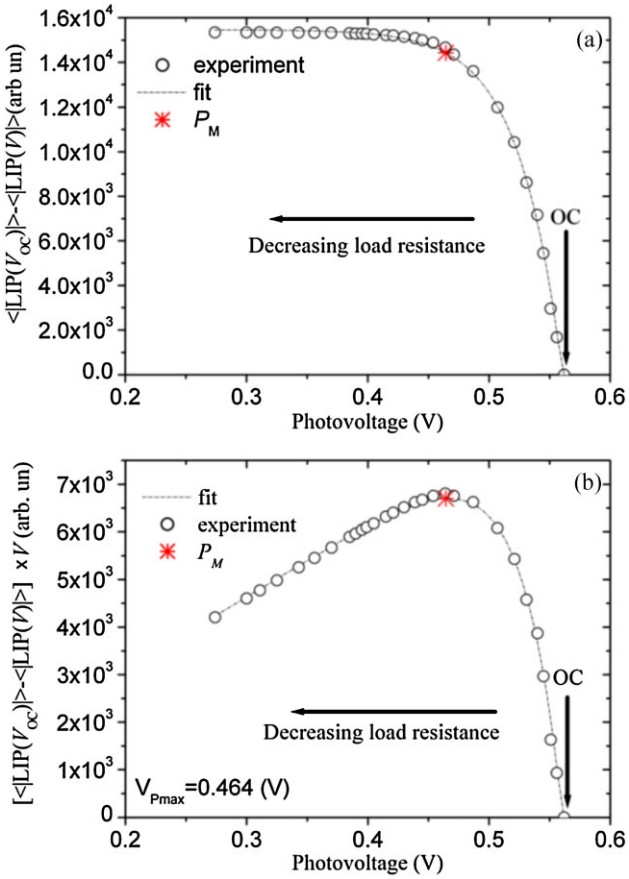

Figure 5 (a) $J[\hbar\omega, V(\hbar\omega), T]_R - V$ characteristics; (b) output power curve. Theoretical fits to Eq. (18) are shown. Illumination power density: 0.038 W cm^{-2}, modulation frequency of 10 Hz.

Furthermore, LIT amplitude images were collected as a function of external load resistance under peak illumination intensity of 0.043 W cm^{-2}. For each value of the load resistance the LIT surface-averaged amplitude, representing the dissipated power flux in the solar cell, was calculated from the corresponding image pixel statistics using Eq. (9). The surface-averaged amplitude curve was fitted to Eq. (12). The parameters A_g, A_0, n, and C in Eq. (12) were determined from the best fit to the data. The values of $\eta\eta_{ce}(\hbar\omega,0,T)$ and the ideality factor n can also be calculated from best fitting the data to the same theoretical curve. Assuming $\eta = 1$ and reflectance $R = 0.05$, the value $\lambda_{em} = 1107$ nm was selected, corresponding to the band gap energy $E_g = 1.12$ eV, and the calibration factor C_{LIT} was calculated from Eq. (11). With C_{LIT} known, the photogenerated current density J_g and saturation diode current density J_0 were obtained from Eqs. (13a) and (13b). The surface-averaged amplitude, the best-fitted theoretical curve and the surface-averaged phase are presented in Fig. 4. The electrical parameter values of the solar cell obtained from LIT imaging are listed in Table 1 and they are in very good agreement with those obtained from independent EM. Although no theoretical best fit to the LIT phase has been attempted in this work because the low frequency used (10 Hz) gave rise to large error bars in the phase, Fig. 4(b). However, it is clear from Fig. 4(a,b) that the LIT amplitude minimum and the phase maximum occur simultaneously at the photovoltage corresponding to the maximum power point, which is consistent with earlier single point measurement results obtained using the photoacoustic gas-cell method [4]. These amplitude-phase extrema can be used for a simple determination of the load resistance associated with the maximum power output of the solar cell. The LIT-calculated photovoltage corresponding to maximum power $V_{pmax} = 0.464$ V was obtained at the minimum value of the surface-averaged amplitude (the lowest dissipated power) in Fig. 4(a).

LIP amplitude images were also obtained for the various external load resistances under the peak illumination intensity condition of 0.038 W cm^{-2}. The surface-averaged

amplitudes representing the radiative recombination emission flux were calculated from the pixel statistics of the images at various external load resistances using Eq. (15a). The $J[\hbar\omega,V(\hbar\omega),T]_R - V$ characteristics, where $J[\hbar\omega, V(\hbar\omega), T]_R$ is given by Eq. (17a), and the best fit to Eq. (18) are shown in Fig. 5(a). The corresponding power curve is shown in Fig. 5(b). From Fig. 5(a) it is seen that the $J[\hbar\omega,V(\hbar\omega),T]_R - V$ characteristic curve is similar to the conventional electrical *I–V* characteristics of Fig. 2(a), thereby validating the optoelectronic Eq. (18). The parameters (J_R, J_{R0}, and n_j) of the radiative recombination emission process in Eq. (18) were determined from the best fit to the data. Assuming the radiative recombination quantum efficiency to be constant, the $\eta_{ce}[\hbar\omega,0,T]$ was calculated from the definitions of radiative and non-radiative quantum efficiencies [26] and Eqs. (5a,b). The corresponding electrical parameters of the solar cell J_g, J_0, n, and V_{OC}, were obtained according to Eqs. (21), (22), and (24) using the best-fitted parameters to Eq. (18) and LIP images. They are listed in Table 1 and they are seen to be in very good agreement with those obtained from the EM. The photovoltage at the maximum power point $V_{pmax} = 0.464$ V was also obtained from the best-fitted curve in Fig. 5(b).

Figures 6 and 7 show the saturation diode current density J_0 and ideality factor n images of the solar cell calculated as derivative images from LIT and LIP images. The J_0 images, scaled in μA cm^{-2}, are shown in Figs. 6(a) and 7(a) using the LIT and LIP images, respectively. For LIT, the ideality factor n image and an intermediate parameter A_0 image were directly obtained from the best fit to Eq. (14). Then, the saturation diode current density J_0 image was derived from Eq. (13a) based on the C_{LIT} image obtained from Eq. (14b). For LIP, the ideality factor n_j image and parameter J_{R0} image were directly obtained from best fitting to Eq. (23a). Then, the ideality factor n image and saturation diode current density J_0 image were derived from Eqs. (24a) and (22), respectively. From the LIT Fig. 6(a), the local saturation diode current density J_0 of the solar cell is variable between 0.1 and 0.2 μA cm^{-2}, and local inhomogeneities are apparent with high contrast. From the LIT Fig. 6(b), the range of local ideality factor n values varies from 1.81 to 1.88, but the ideality factor is less sensitive to local inhomogeneities. Figure 7(a) and (b) show the local characteristics of this solar cell from LIP images. Unlike the LIT-n image, the LIP-n image shows high spatial resolution and contrast that correspond well to the LIP-J_0 image. By comparison, it is seen that at locations where the saturation diode current density is large, the corresponding ideality factor is high. This can be understood from the electrical diode equation as follows: at open-circuit, the

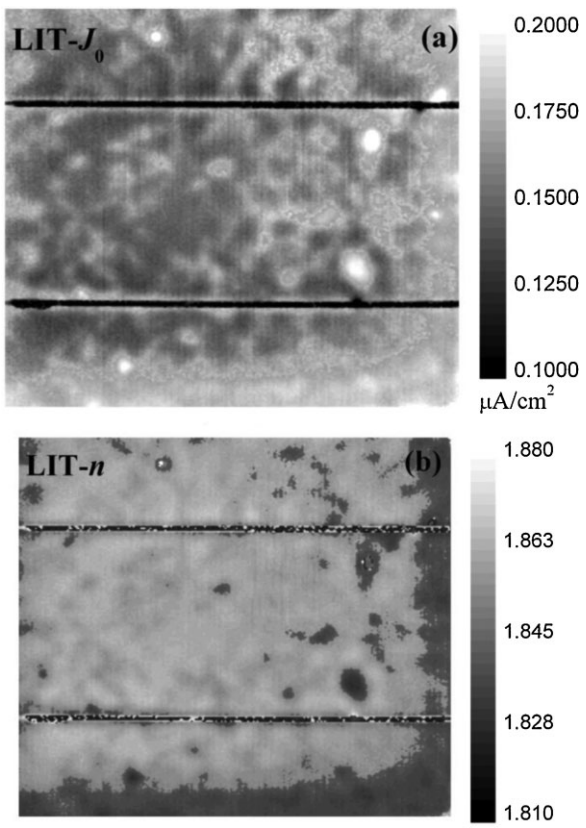

Figure 6 Saturation diode current density J_0 and ideality factor n images using LIT at 10 Hz: (a) LIT-J_0 and (b) LIT-n image, illumination power density: 0.043 W cm^{-2}.

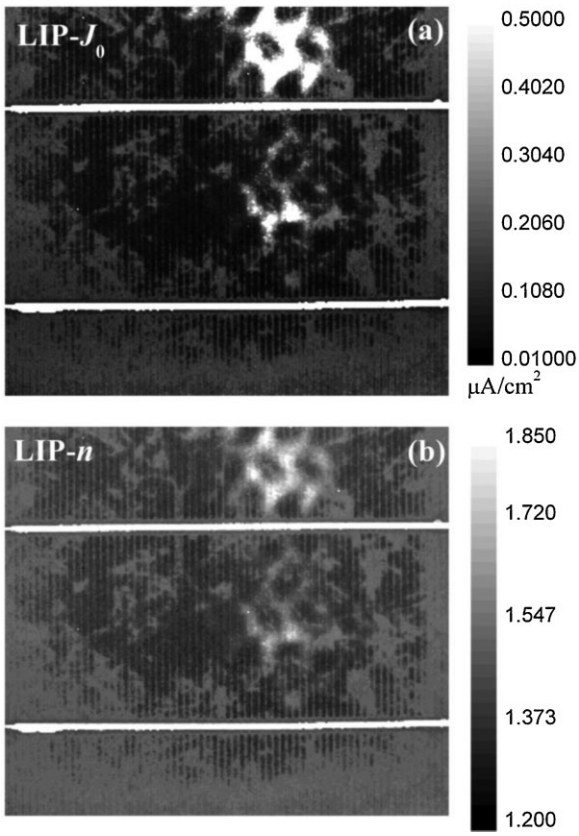

Figure 7 Saturation diode current density J_0 and ideality factor n images using LIP at 10 Hz: (a) LIP-J_0 and (b) LIP-n image, illumination power density: 0.038 W cm^{-2}.

ideality factor $n = \frac{qV_{OC}}{k_B T \ln(J_g/J_0)}$. Given that the photogenerated current density J_g is only related to incident photon flux and current collection efficiency, it can be considered constant under fixed illumination. Therefore, an increase in J_0 yields an increase in n, which is consistent with the results of the two LIP images.

5 Conclusions We have demonstrated that quantitative LIT and LIP imaging and associated pixel statistics can be used to measure several electrical parameters of solar cells. A quantitative theory of the electrical parameter dependence of solar cells on lock-in thermographic and long-pass filtered PL (carrierographic) images was developed. The photogenerated current density J_g, saturation diode current density J_0, ideality factor n, and the photovoltage at maximum power measured from the LIT and LIP images were thus measured. They were found to be in very good agreement with each other and with EM, as a result of theoretical best fits to the surface-averaged pixel brightness values of the two cameras. While LIP has the advantage of higher spatial resolution and contrast, including the derivative J_0 and n images, the combination of quantitative LIT and LIP imaging can yield a more reliable set of electrical parameters of solar cells than either technique alone.

Acknowledgements A. Mandelis is grateful to NSERC for a Discovery grant, to the Canada Foundation for Innovation (CFI) for equipment grants, to the Canada Research Chairs Program, and to the Ontario Ministry for Research and Innovation (MRI) for the Inaugural Premier's Discovery Award in Science and Technology (2007).

Appendix

Symbol and parameter definitions

$A_0 = C_{LIT}J_0$, $A_g = C_{LIT}J_g$, and $C = \frac{\hbar\omega_{in}}{q\eta\eta_{ce}(\hbar\omega,0,T)}$	intermediate parameters
C_{LIT}	calibration factor for LIT
C_{LIC}	calibration factor for LIC
FF	fill factor of solar cell
$F_R(V,T)$	radiative-recombination emission photon flux
$F_i(\hbar\omega)$	incident photon flux
$F_{rec}[\hbar\omega, V(\hbar\omega), T]$	recombination photocarrier flux
F_{NR}	heat flux resulting from the non-radiative conversion of optoelectronic to thermal energy
$F_{ce}[\hbar\omega, V(\hbar\omega), T]$	photocarrier flux collected at the p–n junction that gives rise to photocurrent
$\langle\lvert LIT[V(\omega_M)]\rvert\rangle = \frac{1}{S}\sum_{x=1}^{M}\sum_{y=1}^{N}\lvert LIT[V(\omega_M)]\rvert_{x,y}$	LIT amplitude-averaged
$\langle\lvert LIC[V(\omega_M)]\rvert\rangle = \frac{1}{S}\sum_{x=1}^{M}\sum_{y=1}^{N}\lvert LIC[V(\omega_M)]\rvert_{x,y}$	LIC amplitude-averaged
J_g	photogenerated current density
J_D	injection current density
J_0	saturation diode current density
$J[\hbar\omega,V(\hbar\omega),T]_R$	non-equilibrium radiative recombination current density
$J_R = q\cdot\eta\eta_R(\hbar\omega, V_{OC}, T)F_i(\hbar\omega)$ and $J_{R0} = qF_R(0,T)$	relevant current-like quantities
$\lvert I_i\rvert$	peak value of incident modulated illumination intensity
R	surface reflectance
S	illuminated surface area of the solar cell;
$\lvert T(\omega_M)\rvert$	peak amplitude of modulated surface temperature
T_0	ambient temperature
V_{OC}	open-circuit voltage
$Z(\hbar\omega) = \lvert Z(\hbar\omega)\rvert\cdot e^{i\phi(\hbar\omega)}\cdot e^{i\omega_M t}$	complex quantities
c	speed of light in vacuum
n	electrical ideality factor of solar cell
n_j	optoelectronic ideality factor related to radiative recombination processes
$\alpha(E)$	absorptance and emissivity of solar cell
η	quantum efficiency for carrier photogeneration
η_{ce}	photocarrier-to-current collection efficiency
$\hbar\omega_{in}$	incident photon energy
$\hbar\omega_{em}$	mean radiative-recombination-emission photon energy
η_{NR}	quantum efficiency for non-radiative recombination
η_R	quantum efficiency for radiative recombination
λ_{in}	photon wavelengths corresponding to $\hbar\omega_{in}$
λ_{em}	photon wavelengths corresponding to $\hbar\omega_{em}$

References

[1] D. Cahen, B. Büchner, P. Decker, and M. Wolf, IEEE Trans. Electron Devices **37**(2), 498–508 (1990).
[2] H. Flaisher, M. Wolf, and D. Cahen, J. Appl. Phys. **66**(4), 1832–1841 (1989).
[3] M. Wolf and D. Cahen, Solar Cells **27**, 247–258 (1989).
[4] D. Cahen, Appl. Phys. Lett. **33**(9), 810–811 (1978).
[5] A. Mandelis, J. Appl. Phys. **66**(11), 5572 (1989).
[6] O. Breitenstein and M. Langenkamp, Lock-in Thermography: Basics and Use for Functional Diagnostics of Electric Components (Springer, Berlin, 2003).
[7] O. Breitenstein, W. Warta, and M. Langenkamp, Lock-in Thermography: Basics and Use for Evaluating Electronic Devices and Materials, 2nd ed. (Springer, Berlin, 2010).
[8] H. Straube, J. M. Wanger, J. Schneider, and O. Breitenstein, J. Appl. Phys. **110**, 084513 (2011).
[9] O. Breitenstein, M. Langenkamp, and M. H. A. Rifai, Prog. Photovolt. **11**, 515 (2003).
[10] O. Breitenstein, M. Langenkamp, O. Lang, and A. Schirrmacher, Sol. Energy Mater. Sol. Cells **65**, 55 (2001).
[11] O. Breitenstein, J. P. Rakotoniaina, M. H. A. Rifai, and M. Weren, Prog. Photovolt. **12**, 529 (2004).
[12] O. Breitenstein and J. P. Rakotoniaina, J. Appl. Phys. **97**, 074905 (2005).
[13] J. Isenberg and W. Warta, J. Appl. Phys. **95**, 5200 (2004).
[14] H. Straube, J. M. Wanger, and O. Breitenstein, Appl. Phys. Lett. **95**, 052107 (2009).
[15] M. Kasemann, B. Walter, C. Meihardt, J. Ebser, W. Kwapil, and W. Warta, J. Appl. Phys. **103**, 113503 (2008).
[16] T. Trupke, R. A. Bardos, M. D. Abbott, and J. E. Cotter, Appl. Phys. Lett. **87**, 093503 (2005).
[17] T. Trupke, R. A. Bardos, M. C. Schubert, and W. Warta, Appl. Phys. Lett. **89**, 044107 (2006).
[18] T. Trupke, J. Appl. Phys. **100**, 063531 (2006).
[19] D. Macdonald, J. Tan, and T. Trupke, J. Appl. Phys. **103**, 073710 (2008).
[20] J. Giesecke, M. Kasemann, and W. Warta, J. Appl. Phys. **106**, 014907 (2009).
[21] D. Kiliani, G. Micard, B. Setuer, B. Raabe, A. Herguth, and G. Hahn, J. Appl. Phys. **110**, 054508 (2011).
[22] B. Michl, D. Impera, M. Bivour, W. Warta, and M. C. Schubert, Prog. Photovolt. Res. Appl., DOI: 10.1002/pip.2293 (2012).
[23] A. Mandelis, J. Batista, and D. Shaughnessy, Phys. Rev. B **67**, 205208 (2003).
[24] A. Melnikov, A. Mandelis, J. Tolev, P. Chen, and S. Huq, J. Appl. Phys. **107**, 114513 (2010).
[25] A. Melnikov, A. Mandelis, J. Tolev, and E. Lioudakis, J. Phys.: Conf. Ser. **214**, 012111 (2010).
[26] A. Mandelis, Y. Zhang, and A. Melnikov, J. Appl. Phys. **112**, 054505 (2012).
[27] P. Würfel, J. Phys. C. **15**, 3967 (1982).
[28] D. Shaughnessy and A. Mandelis, Rev. Sci. Instrum. **74**, 529 (2003).
[29] T. Kirchartz and U. Rau, Phys. Status Solidi A **205**(12), 2737 (2008).
[30] U. Rau, IEEE J. Photovolt. **2**(2), 169–172 (2012).
[31] J. Nelson, The Physics of Solar Cells (Imperial College Press, London, 2003), Chaps. 4, 6.
[32] A. K. Ghosh, C. Fishman, and T. Teng, J. Appl. Phys. **51**, 446 (1980).